Supporting Information

Aggregation-induced structural clamping drives NIR photoluminescence switching in Au_2Cu_6 nanoclusters by suppressing El-Sayed-allowed intersystem crossing

Hayato Yamauchi, Daichi Arima, Masaaki Mitsui*

Department of Chemistry, College of Science, Rikkyo University, 3-34-1, Nishiikebukuro, Toshima-ku, Tokyo 171-8501, Japan

Corresponding author

*E-mail: mitsui@rikkyo.ac.jp

Chemicals

Hydrogen tetrachloroaurate(III) tetrahydrate ($HAuCl_4 \cdot 4H_2O$), copper(I) chloride (CuCl), and tetrahydrofuran (THF) were obtained from FUJIFILM Wako Pure Chemical Corporation. Platinum(II) octaethylporphine (PtOEP), *N,N'*-bis(2,5-di-*tert*-butylphenyl)-3,4,9,10-perylenedicarboximide (PDI), 1-adamantanethiol (Adm-SH), methanol (MeOH), *n*-hexane, toluene, and ethanol (EtOH) were purchased from Sigma-Aldrich. Sodium borohydride ($NaBH_4$), triphenylphosphine (PPh_3), tri(*p*-tolyl)phosphine [$P(PhMe)_3$], and perylene were purchased from Tokyo Chemical Industry Co., Ltd. All chemicals were used as received without further purification. Ultrapure water (≥18.2 MΩ·cm) was obtained using a Direct-Q UV distillation system.

Synthesis of $Au_2Cu_6(S\text{-}Adm)_6[P(PhMe)_3]_2$ and $Au_2Cu_6(S\text{-}Adm)_6(PPh_3)_2$

$Au_2Cu_6(S\text{-}Adm)_6[P(PhMe)_3]_2$ (**Au_2Cu_6PhMe**) and $Au_2Cu_6(S\text{-}Adm)_6(PPh_3)_2$ (**Au_2Cu_6Ph**) were prepared by adapting the previously reported synthetic protocol for **Au_2Cu_6Ph**,[1] with minor modifications. CuCl (25 mg, 0.25 mmol) was first dissolved in a 1:1 (v/v) mixture of methanol and acetonitrile, after which Adm-SH (136 mg, 0.8 mmol) was added. The mixture was stirred until a homogeneous, colorless solution was obtained. Separately, $Au(P(PhMe)_3)Cl$ or $Au(PPh_3)Cl$ was generated in situ by dissolving $HAuCl_4$ (12 mg, 0.036 mmol) and $P(PhMe)_3$ (19.0 mg, 0.06 mmol) or PPh_3 (15.8 mg, 0.06 mmol) in toluene (5 mL). This resulting gold precursor solution was added dropwise to the copper–1-adamantanethiolate solution, followed by the addition of an aqueous $NaBH_4$ solution (1 mL, 80 mg mL^{-1}) to initiate reduction. The reaction mixture was stirred at room temperature for 24 h, during which a precipitate formed. The precipitate was collected by centrifugation and washed successively with *n*-hexane, ethanol, and methanol. Subsequent extraction with THF afforded **Au_2Cu_6PhMe** (12 mg, 0.005 mmol) or **Au_2Cu_6Ph** (22 mg, 0.01 mmol). The isolated yields correspond to 27 % or 53%, respectively, based on the amount of gold atoms employed.

The purified product was diluted in a THF/MeOH mixture and analyzed by positive-mode electrospray ionization mass spectrometry (ESI-MS) using a JEOL JMS-T100LP AccuTOF LC-Plus spectrometer. As shown in Fig. S1, a prominent peak was observed at m/z ≈ 2,387, which is attributable to the **Au_2Cu_6PhMe** nanocluster ion (calcd m/z = 2,387.7). The experimentally obtained isotopic pattern shows excellent agreement with the simulated distribution, thereby confirming the nanocluster composition. Single crystals suitable for X ray diffraction analysis were grown by slow vapor diffusion of *n*-hexane into a THF solution of the purified compound over two days.

Single crystal X-ray diffraction measurement

Single-crystal X-ray diffraction (SC-XRD) data were collected at 173 K on a Bruker D8 QUEST diffractometer equipped with a PHOTON III area detector, using Mo Kα radiation (λ = 0.71073 Å). The structures were solved by dual-space methods using SHELXT (version 2018/2) and refined by full-matrix least-squares procedures on F^2 with SHELXL (version 2018/3), as implemented in the Olex2 1.3 software package. All non-hydrogen atoms were refined with anisotropic displacement parameters. Hydrogen atoms were placed in geometrically calculated positions (C–H = 0.93 Å for aryl groups and 0.97 Å for alkyl groups) and refined using a riding model. The crystal structures of **Au_2Cu_6PhMe** and the corresponding crystallographic parameters are presented in Fig. S2 and Table S1. The structure was visualized using Mercury (version 2025.3.3).

Theoretical calculations

All density functional theory (DFT) and time-dependent DFT (TD-DFT) calculations were performed using the Gaussian 16 software package (ES64L-G16, Rev. B.01).[2] The geometric and electronic structures of **Au_2Cu_6PhMe** were investigated without ligand simplification. Because ligand–ligand interactions on the metal core surface play a crucial role in stabilizing the metal framework, truncation of ligands can significantly perturb metal–metal distances and bond angles, potentially altering the Kohn–Sham orbitals and excited-state properties relative to the full structure. Therefore, all ground- and excited-state calculations were carried out using the complete molecular structure.

Geometry optimizations were performed for the ground state (S_0) and excited states (S_1 and T_1) using the PBE0 functional.[3] combined with Grimme's empirical dispersion correction (GD3).[4] The def2-SV(P) basis sets were employed for Au and Cu atoms,[5] while the 6-31G(d) basis sets were applied to H, C, O, and S atoms.[6] Scalar relativistic effects were accounted for using the Stuttgart/Dresden (SDD) effective core potentials.[7] All optimized structures were confirmed to be true local minima by harmonic vibrational frequency analysis, with no imaginary frequencies observed. In the structural optimization of **Au_2Cu_6PhMe** under C_i symmetry, the crystal structure was employed as the initial geometry, and geometry optimization was carried out under the C_i symmetry constraint. The resulting structure does not correspond to a true minimum on the potential energy surface, as the optimization was performed for an isolated nanocluster. ZORA-TD-DFT calculations mentioned below were subsequently performed using this optimized structure. Because direct optimization of the T_2 state was not feasible, the S_1–T_2 energy gap was estimated from vertical transition energies. Specifically, the S_1–S_0 and T_2–S_0 transition energies were calculated at the optimized S_1 geometry, and their difference was taken as the S_1–T_2 energy gap. Geometries and molecular orbitals were visualized using GaussView 6.0 and Avogadro

1.2.0.

Spin–orbit coupling (SOC) matrix elements were calculated using ORCA 5.0.4 at the TD-B3LYP level,[8,9] incorporating scalar relativistic effects through the zeroth-order regular approximation (ZORA) Hamiltonian.[10,11] To accelerate the SOC integral evaluation, the RI-SOMF(1X) approximation was employed, and the Tamm–Dancoff approximation (TDA) was disabled to enable full TD-DFT calculations. Grimme's DFT-D3 empirical dispersion corrections were included to account for dispersion interactions.[12] For SOC calculations, the SARC-ZORA-TZVP basis sets were used for Au atoms, while ZORA-def2-SVP basis sets were applied to C, H, and S atoms.[13] Solvent effects were incorporated using the conductor-like polarizable continuum model (C-PCM).[14]

Absorption and emission measurements

Ultraviolet–visible absorption spectra were recorded using either a Lambda 650 spectrometer (PerkinElmer) over the wavelength range of 300–800 nm with 1 nm resolution. Visible and near-infrared (NIR) emission spectra were obtained by collecting the emission signal from the sample solution via an optical fiber into a CCD spectrometer (Ocean SR6 or USB4000, Ocean Insight). The spectral sensitivity of spectrometers was calibrated using a standard light source (HL-3P-INT-CAL, Ocean Photonics) under optical conditions identical to those employed during the measurements.

Time-resolved emission measurements and analysis

Details of the experimental setup for time-resolved emission measurements have been described in our previous reports.[10–13] Time-resolved experiments were conducted using either a home-built time-correlated single-photon counting (TC-SPC) system or the TC-SPC mode of a PicoTAS setup (UNISOKU Co., Ltd.). In the custom-built system, excitation was provided by a 478 nm picosecond pulsed laser (pulse width: 80 ps; PiL048X, Advanced Laser Diode Systems), and emission decays were detected using an avalanche photodiode (APD, SPCM-AQRH-61, PerkinElmer) coupled with a TC-SPC module (TimeHarp 260, PicoQuant). Data analysis was carried out using SymPhoTime 64 software (PicoQuant). All emission measurements were conducted in THF solutions thoroughly degassed with high-purity argon gas (>99.999%).

The PL decay curves were fitted using double-exponential functions as follows:

$$I(t) = \sum_{i=1}^{2} A_i \exp\left(-\frac{t}{\tau_i}\right) \tag{S1}$$

where A_i represents the normalized amplitude of species *i*, and τ_i is the lifetime of species *i*. The fractional population (f_i) was calculated by the following equation:

$$f_i = \frac{A_i \tau_i}{\sum_{i=1}^{2} A_i \tau_i} \,. \tag{S2}$$

Evaluation of PL and UC quantum yields by relative method

The relative Φ_{PL} and Φ_{UC} was calculated using the following equation:

$$\Phi_{PL} = \frac{I_r\left(1 - 10^{-A_r(\lambda_{ex})}\right)}{I_s\left(1 - 10^{-A_s(\lambda_{ex})}\right)} \frac{\int F_s(\lambda_{em})\, d\lambda_{em}}{\int F_r(\lambda_{em})\, d\lambda_{em}} \frac{{n_s}^2}{{n_r}^2} \Phi_f^r, \tag{S3}$$

where Φ_f^r represents the known fluorescence quantum yield of the reference dye, A, F, and I represent the absorbance at the excitation wavelength (l_{ex}), the PL intensity, and excitation laser intensity, respectively, and n is the refractive index of the corresponding solvent. PDI (Φ_f = 0.97 in toluene)[15] was used as a standard for 532 nm excitation. The fluorescence (Φ_{FL}) and phosphorescence (Φ_{PH}) quantum yields were determined by deconvoluting the respective PL bands and multiplying their integrated area fractions by the total PL quantum yield.

Dynamic light scattering measurements

Dynamic light scattering (DLS) analyses were carried out using a nanoSAQLA instrument (Otsuka Electronics Co., Ltd.). Measurements were performed at 25 °C with a 660 nm laser as the excitation source. The particle size distributions were obtained from analysis of the intensity autocorrelation function, $G^{(2)}(t)$, of the scattered light using the nanoSAQLA software. Solvent parameters, including viscosity and refractive index, were appropriately set for the analysis.

Triplet energy transfer (TET) quantum yield

The TET quantum yield (Φ_{TET}) can be estimated by performing quenching measurements of the PL lifetimes of the sensitizer, as described by the Stern-Volmer relationship as follows:

$$\frac{\tau_0}{\tau} = 1 + K_{SV}[\mathrm{Em}], \tag{S4}$$

where K_{SV} is the Stern–Volmer constant, [Em] is the emitter concentration, and τ_0 and τ correspond to the unquenched and quenched PL lifetimes of the sensitizer, respectively. In the present case, τ_0 corresponds to the phosphorescence lifetime of **Au_2Cu_6PhMe**. The Φ_{TET} was calculated by the following equation:

$$\Phi_{TET} = \frac{K_{SV}[\mathrm{Em}]}{1 + K_{SV}[\mathrm{Em}]} = \frac{k_{TET}\tau_0[\mathrm{Em}]}{1 + k_{TET}\tau_0[\mathrm{Em}]} \tag{S5}$$

Estimation of the ISC quantum yield of Au_2Cu_6PhMe in solution

To determine the ISC quantum yield (Φ_{ISC}) of **Au_2Cu_6PhMe** in THF, a relative method using triplet–triplet annihilation upconversion (TTA-UC) was employed.[16,17] In the TTA-UC, the formation yield of the upconverted S_1 state of the emitter (Φ_{UCs}), defined as the number of upconverted emitter S_1
states generated per initially formed sensitizer S_1 state, is expressed as: [18]

$$\Phi_{UCs} = \Phi_{ISC}\Phi_{TET}\frac{f}{2}\Phi_{TTA} \tag{S6}$$

where Φ_{ISC} is the intersystem crossing yield of the sensitizer, Φ_{TET} is the quantum yield of TET from the sensitizer to the emitter, and f is the spin statistical factor of the emitter, and Φ_{TTA} is the quantum yield of TTA between emitter triplets.

Experimentally, Φ_{UCs} cannot be obtained directly but can be evaluated from the observed upconversion quantum yield (Φ_{UC}) by correcting for optical and kinetic loss processes. Specifically, reabsorption and outcoupling losses of upconverted photons are accounted for by the optical outcoupling yield (Φ_{out}), and quenching yield of emitter triplets

by the sensitizer is described by the quenching yield (Φ_q). The relationship between Φ_{UCs} and Φ_{UC} is therefore given by: [18]

$$\Phi_{UCs} = \frac{\Phi_{UC}}{\Phi_{out}(1-\Phi_q)\Phi_{FL}} \tag{S7}$$

where Φ_{FL} is the fluorescence quantum yield of the emitter.

When the same emitter is employed in both the target and reference TTA-UC systems, taking the ratio of eq S6 for the sample and the reference (r) eliminates the terms related to the emitter, namely $f\Phi_{TTA}/2$:

$$\frac{\Phi_{UCs}}{\Phi^r_{UCs}} = \frac{\Phi_{ISC}\Phi_{TET}}{\Phi^r_{ISC}\Phi^r_{TET}} \tag{S8}$$

On the basis of eq S7, this ratio can be experimentally evaluated as:

$$\frac{\Phi_{UCs}}{\Phi^r_{UCs}} = \frac{\Phi_{UC}/\Phi_{out}(1-\Phi_q)}{\Phi^r_{UC}/\Phi^r_{out}(1-\Phi^r_q)} \tag{S9}$$

By combining eqs S8 and eq S9, the Φ_{ISC} of the sensitizer of interest can be determined according to: [16,17]

$$\Phi_{ISC} = \frac{\Phi^r_{ISC}\Phi^r_{TET}}{\Phi_{TET}} \cdot \frac{\Phi_{UC}\Phi^r_{out}(1-\Phi^r_q)}{\Phi^r_{UC}\Phi_{out}(1-\Phi_q)} \tag{S10}$$

Here, Φ^r_{ISC}, Φ^r_{TET}, Φ^r_{UC}, and Φ^r_q represent the ISC, TET, UC, and quenching quantum yields of the reference sensitizer, respectively. PtOEP (Φ^r_{ISC} = 1) was used as a reference for 532 nm excitation, with perylene used as the emitter. All Φ_{UC} values were evaluated under identical experimental conditions, including emitter concentration, solvent, optical setup, and excitation wavelength. The Φ_{TET} values were independently determined by Stern–Volmer analysis.

The optical outcoupling yield (Φ_{out}) and quenching yield (Φ_q) were evaluated as follows. To determine Φ_q, the emitter triplet lifetime (τ_T) was extracted at each sensitizer concentration by fitting the time-resolved UC emission decay, $I(t)$, using the expression: [19]

$$I(t) = I(0)\left(\frac{1-\beta}{\exp(t/\tau_T)-\beta}\right)^2 \tag{S11}$$

where

$$\beta = \frac{2k_{TTA}[^3Em^*]_0}{1/\tau_T + 2k_{TTA}[^3Em^*]_0} \qquad (0 < \beta < 1). \tag{S12}$$

Here, k_{TTA} is the TTA rate constant and $[^3Em^*]_0$is the initial concentration of emitter triplets. The UC decay curves measured at different sensitizer concentrations, together with the extracted τ_T and β values, are summarized in the Supporting Information.

The reciprocal triplet lifetime was then plotted as a function of sensitizer concentration [Sen] to construct Stern–Volmer plots, which follow:

$$\frac{1}{\tau_T} = \frac{1}{\tau_{T0}} + k_q[\text{Sen}]. \tag{S13}$$

where τ_{T0} is the intrinsic emitter triplet lifetime in the absence of sensitizer and k_q is the bimolecular quenching rate constant. The quenching efficiency Φ_q was subsequently calculated using:

$$\Phi_q = \frac{k_q\tau_{T0}[\text{Sen}]}{1 + k_q\tau_{T0}[\text{Sen}]}. \tag{S14}$$

Estimation of the ISC quantum yield of Au_2Cu_6PhMe in aggregated states

Since the direct experimental determination of Φ_{ISC} is challenging for solid samples (powder and crystals), we determined these values based on the following kinetic analysis. We observed that the radiative rate constant of fluorescence (k_r^{FL}) remains nearly constant between the solution and solid states (Table 1). In **Au_2Cu_6PhMe**, both fluorescence and phosphorescence predominantly originate from the metal-core-centered HOMO-LUMO transitions (Fig.4a and Table S9). Therefore, the environmental insensitivity of k_r^{FL} indicates that the transition dipole moments are not significantly perturbed by the change from a solvent environment to a crystal lattice. Based on this, it is reasonable to assume that the intrinsic radiative rate of phosphorescence (k_r^{PH}) also remains comparable across these states. Using the k_r^{PH} value obtained in THF (5.3×10^4 s^{-1}) and the experimentally measured τ_{PH} for the aggregated states, we determined the triplet emission efficiency, Φ_p (where $\Phi_p = k_r^{PH} \times \tau_{PH}$). Subsequently, Φ_{ISC} was calculated as Φ_{PH}/Φ_p.

Theoretical estimation of ISC rate constant

The ISC rate constant (k_{ISC}) was estimated using the ISC rate expression based on the Marcus semiclassical theory.[20,21] The parameters were derived from the ZORA/TD-DFT calculations mentioned above.

$$k_{ISC} = \frac{2\pi}{\hbar} |V_{SO}|^2 \frac{1}{\sqrt{4\pi\lambda_{RE} k_B T}} \exp\left(-\frac{(\Delta E_{ST} + \lambda_{RE})^2}{4\lambda_{RE} k_B T}\right), \quad \text{(S15)}$$

where the ΔE_{ST} is the adiabatic energy gap between the singlet and triplet states and λ_{RE} is the reorganization energy. To account for the contributions of the three spin-sublevels in the triplet state, $|V_{SO}|^2$ was averaged using the following equation:

$$|V_{SO}|^2 = \frac{\left|\langle T_n|\hat{H}_{SO}|S_1\rangle\right|^2}{3} = \frac{1}{3}\sum_{i\,=\,x,y,z} \left|\langle T_n|\hat{H}_{SO\,i}|S_1\rangle\right|^2. \quad \text{(S16)}$$

Computational details for RMSD analysis

To quantitatively evaluate the structural similarities and discrepancies among the optimized geometries of the S_0, S_1, and T_1 states, root-mean-square deviation (RMSD) values were calculated for all 250 atoms of the **Au_2Cu_6PhMe** nanocluster. The RMSD was determined using the 3D Cartesian coordinates (x, y, z) obtained from the DFT and TD-DFT calculations. Before calculating the deviations, a least-squares superposition (Kabsch algorithm) was performed to minimize the distances between corresponding atoms by accounting for translational and rotational degrees of freedom. The total RMSD was computed according to the following equation:

$$RMSD = \sqrt{\frac{1}{N}\sum_{i=1}^{N} \delta_i^2}. \quad \text{(S17)}$$

where N represents the total number of atoms (N = 250) and δ_i is the distance between the i-th atom in the two compared structures after optimal alignment. The analysis was further

partitioned into the "Metal Core" (8 atoms) and "Ligand" (242 atoms) to clarify the local structural contributions to the overall electronic transitions.

Supplementary Figures

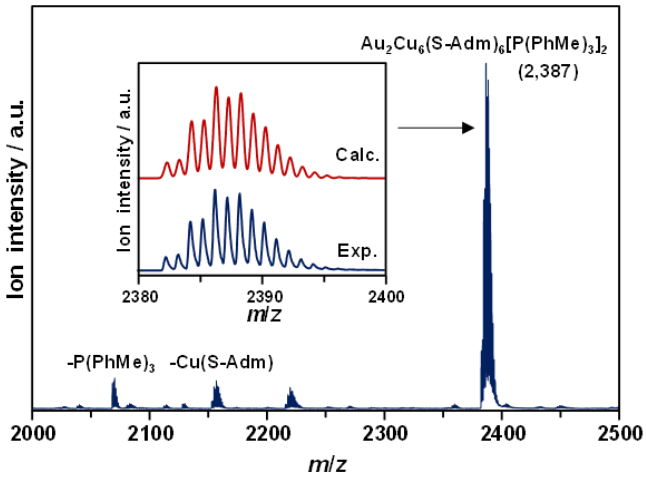

Fig. S1 Positive-ion mode ESI-mass spectrum of $Au_2Cu_6(S\text{-}Adm)_6(P(PhMe)_3)_2$ (**Au_2Cu_6PhMe**) in THF/MeOH. The daughter ions of Cu(S-Adm) or $P(PhMe)_3$ dissociated from the parent ion were also observed.

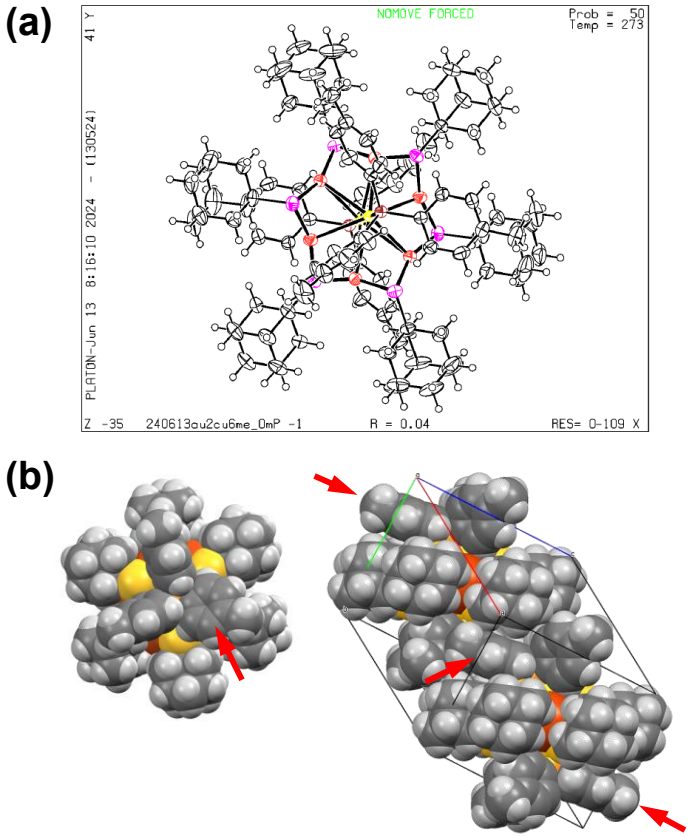

Fig. S2 (a) Thermal ellipsoid representation of the molecular structure of $C_{102}H_{132}Au_2Cu_6P_2S_6$ (**Au_2Cu_6PhMe**) determined by single-crystal X-ray diffraction. (b) Space-filling model of derived from the SC-XRD structure. Red arrows indicate the tolyl (PhMe) moieties that undergo significant conformational rotations to accommodate

intermolecular packing interactions relative to the solution-state D_{3d}-like structure. The left image shows a perspective along the P-Au-Au-P backbone, and the right image provides a viewpoint highlighting the distorted packing within the crystal lattice.

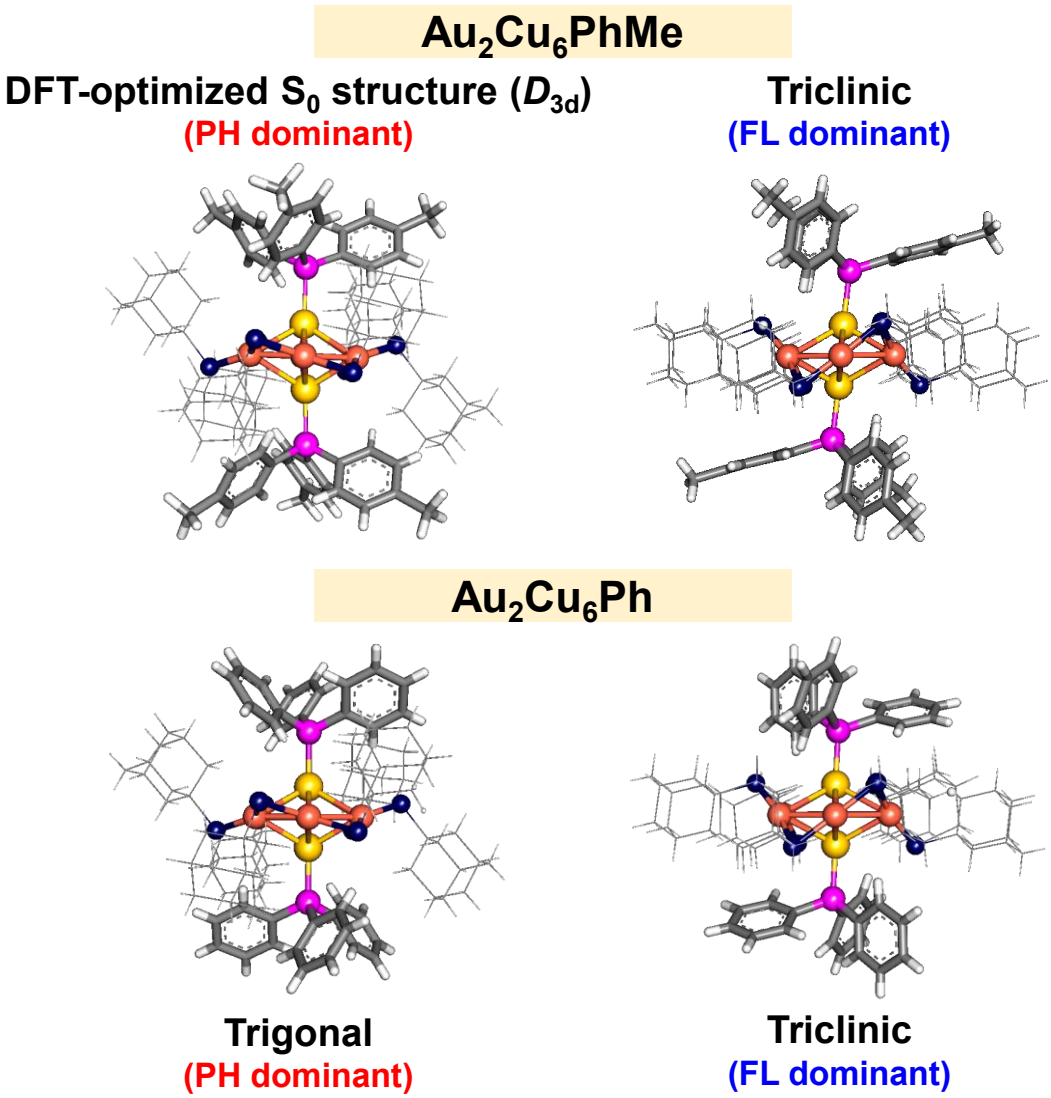

Fig. S3. Comparison of the Au_2Cu_6-based nanocluster geometries: (Upper) DFT-optimized S_0 structure (with D_{3d}-like symmetry in solution) and the observed triclinic polymorph of **Au_2Cu_6PhMe** (this work). (Lower) Reported trigonal and triclinic polymorphs of **Au_2Cu_6Ph** (reproduced from Ref. 22). Notably, a high degree of structural similarity is observed between the DFT-optimized S_0 structure and trigonal polymorph, as well as between the two triclinic structures of **Au_2Cu_6PhMe** and **Au_2Cu_6Ph**. The distinct correlation between geometry (specifically symmetry lowering in the triclinic forms) and the dominant emission process—fluorescence (FL) versus phosphorescence (PH)—is visually evident.

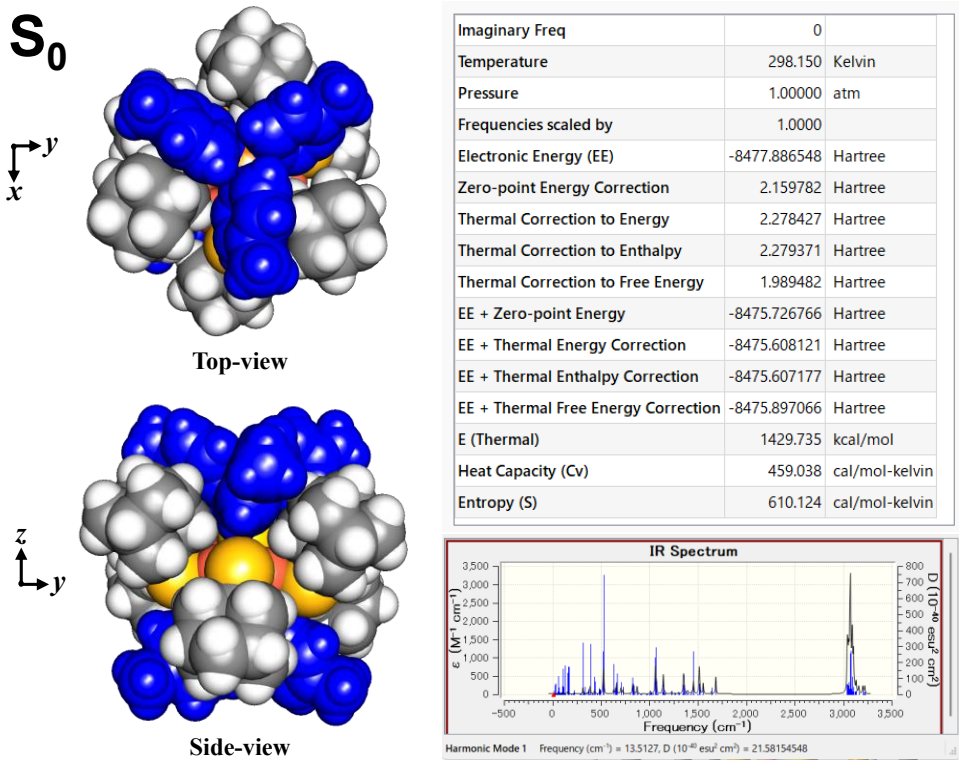

Fig. S4 Optimized structures of **Au_2Cu_6PhMe** in the S_0, S_1, and T_1 states and the corresponding energies and infrared spectra obtained by the normal mode analysis.

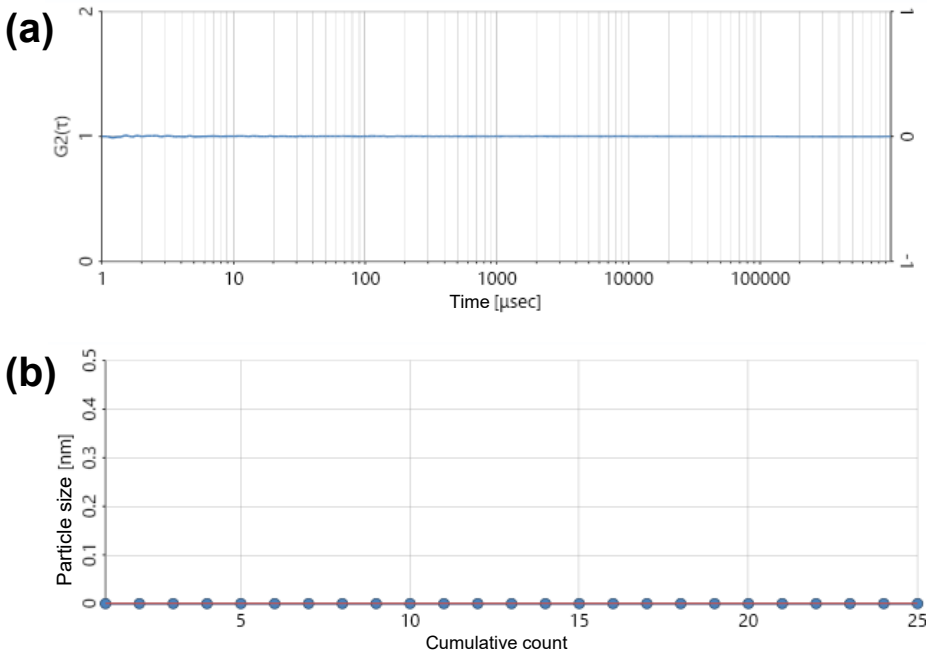

Fig. S5 (a) Intensity autocorrelation function, $G^{(2)}(\tau)$, of the scattered light, and (b) the particle diameter as a function of accumulation number obtained by DLS measurements for THF solutions of **Au_2Cu_6PhMe** (1 µM). No signal of the scattering autocorrelation function was observed, and the average particle diameter remained zero throughout the measurements, indicating the absence of aggregate formation.

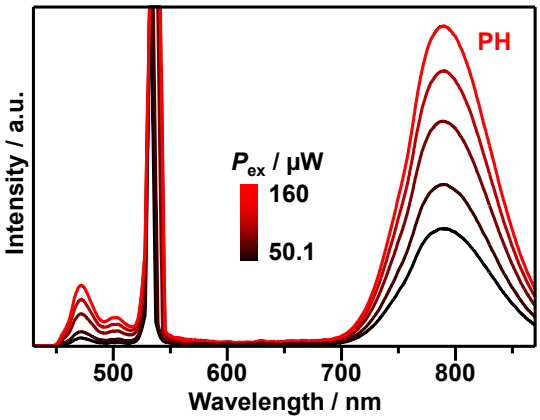

Fig. S6 Excitation power-dependent UC emission spectra of **Au_2Cu_6PhMe** (5.7 µM) and perylene (5 mM) in deaerated THF (λ_{ex} = 532 nm).

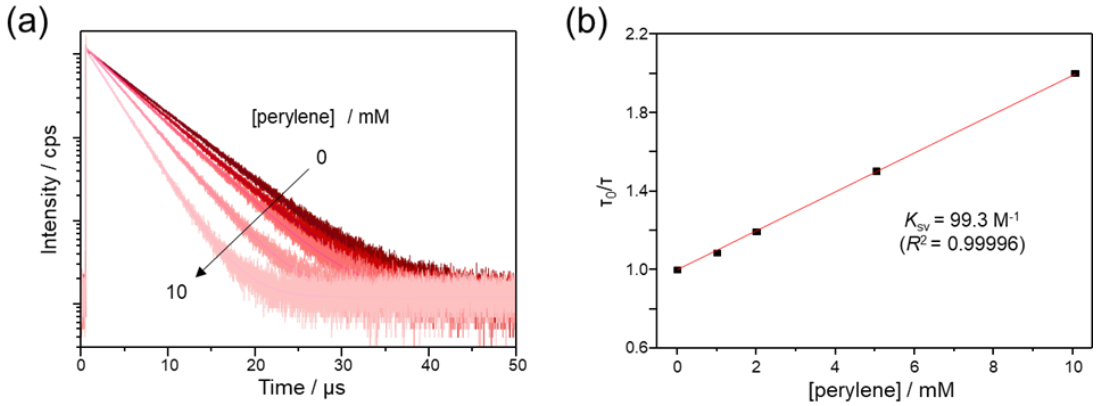

Fig. S7 (a) PL decay curves of **Au_2Cu_6PhMe** (10 μM) with [perylene] = 0–10 mM in deaerated THF (λ_{ex} = 478 nm). (b) Stern–Volmer plots of PL quenching of **Au_2Cu_6PhMe** by perylene.

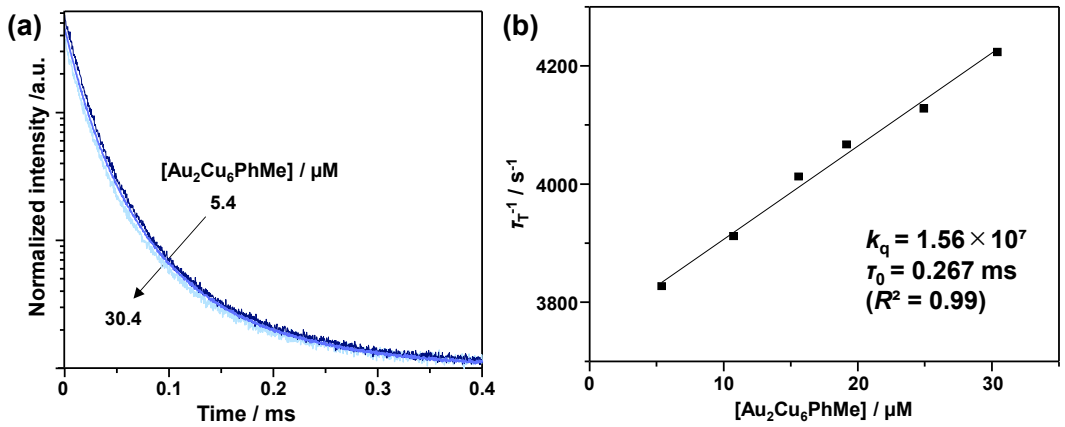

Fig. S8 (a) UC decay curves of solutions containing different concentrations of **Au_2Cu_6PhMe** with 5.0 mM perylene (λ_{ex} = 532 nm). (b) Stern-Volmer plot of UC emission quenching.

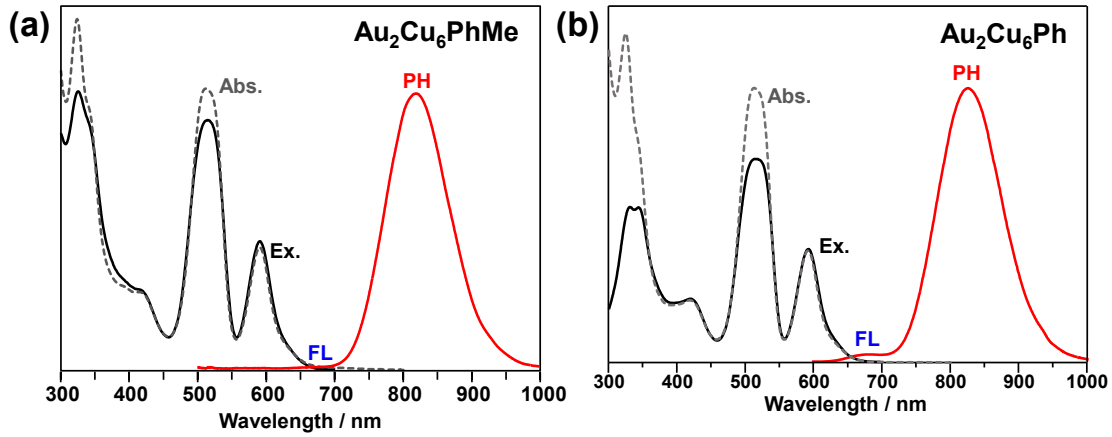

Fig. S9. Absorption (Abs), excitation (Ex), and emission spectra of (a) **Au_2Cu_6PhMe** and (b) **Au_2Cu_6Ph** in deaerated THF. The excitation spectra were observed by monitoring at 710 ± 5 nm.

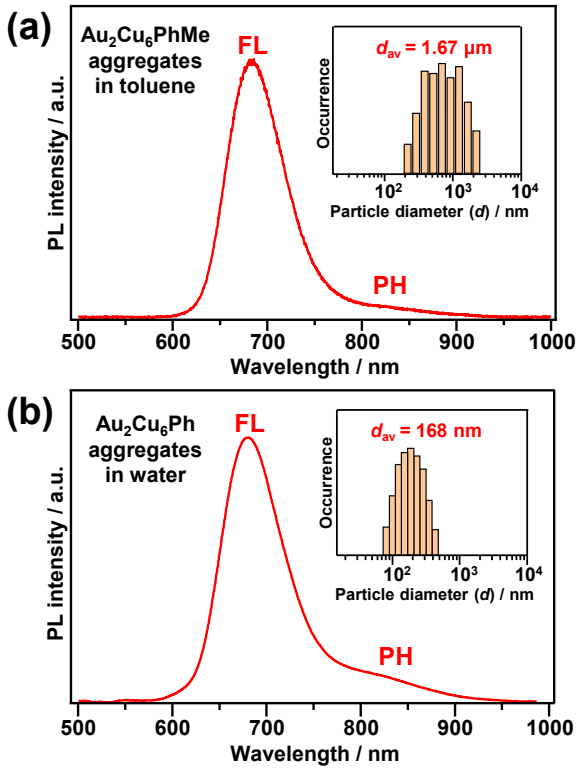

Fig. S10 Emission spectra of aggregated (a) **Au_2Cu_6PhMe** and (b) **Au_2Cu_6Ph** dispersed in toluene and water, respectively. Insets show particle size distributions of the aggregates obtained by dynamic light scattering.

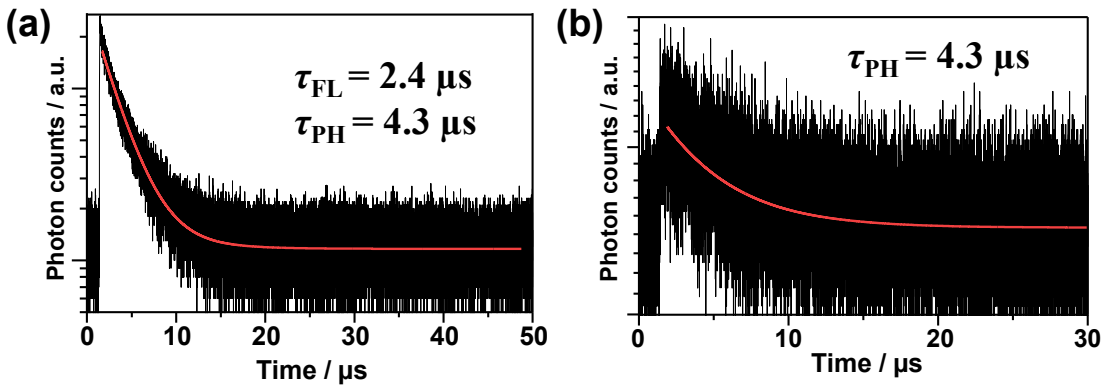

Fig. S11 Time-resolved PL decay profiles of **Au_2Cu_6PhMe** in the crystalline state (λ_{ex} = 478 nm) obtained by monitoring (a) the total emission and (b) the PH signal ($\lambda \geq 800$ nm). In (b), the PH rise was not observable due to the low signal-to-background ratio and the overlapping contribution of the intense FL component in the early-time region. Red lines represent the fitting curves.

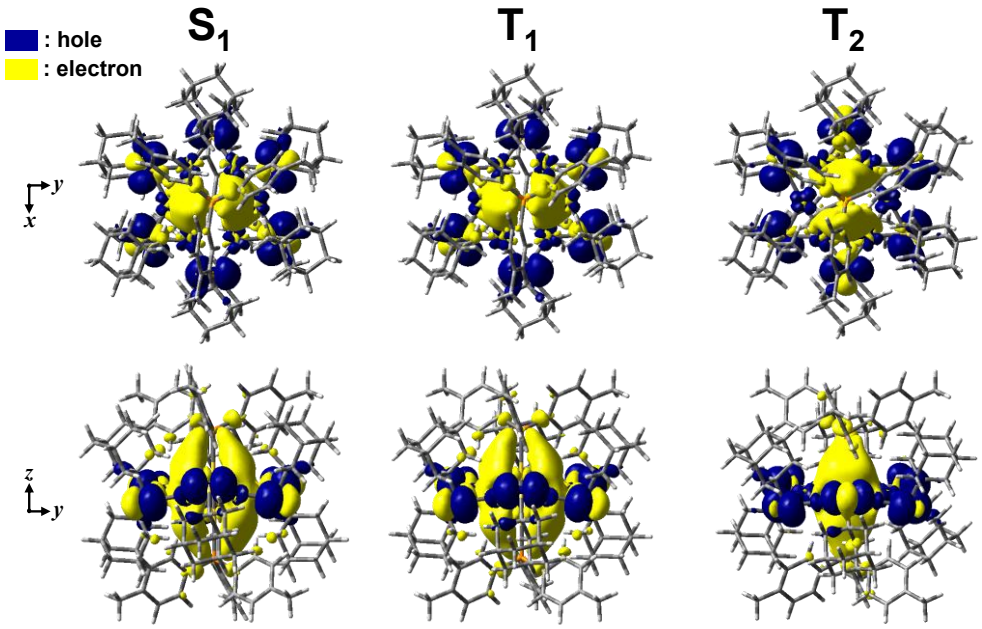

Fig. S12 The hole and electron distributions of the S_1, T_1, and T_2 states obtained at the S_1- and T_1-optimized structures of **Au_2Cu_6PhMe**. There is a clear orthogonality between the electron distributions of S_1 and T_2.

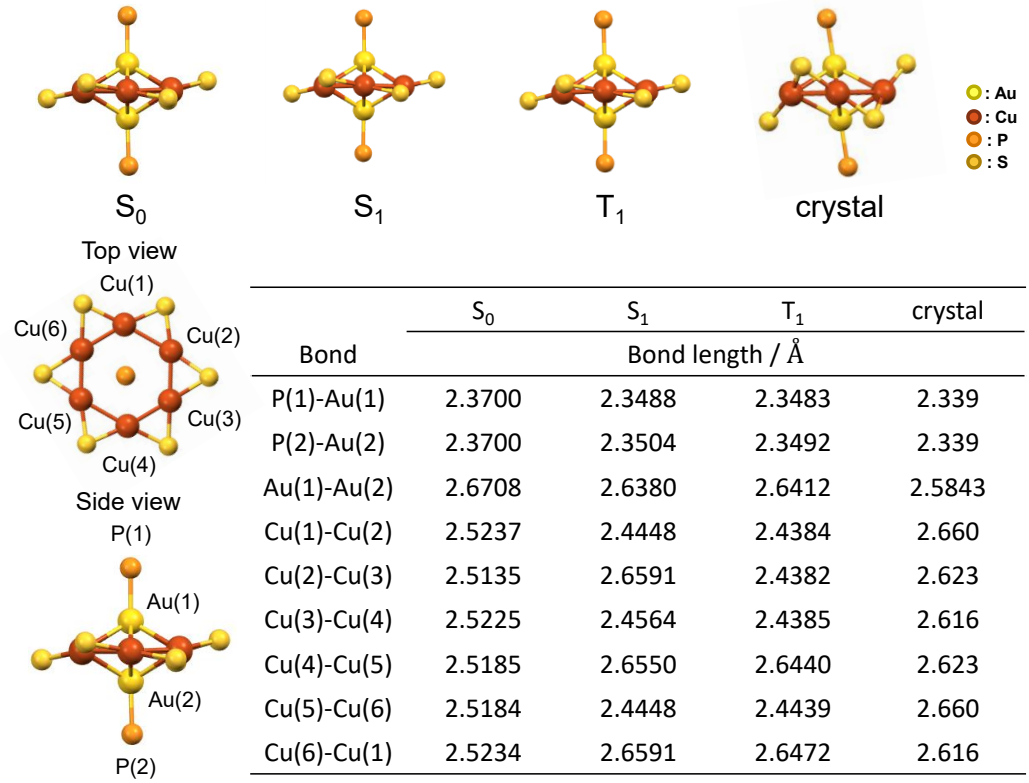

Bond	S_0	S_1	T_1	crystal
	Bond length / Å			
P(1)-Au(1)	2.3700	2.3488	2.3483	2.339
P(2)-Au(2)	2.3700	2.3504	2.3492	2.339
Au(1)-Au(2)	2.6708	2.6380	2.6412	2.5843
Cu(1)-Cu(2)	2.5237	2.4448	2.4384	2.660
Cu(2)-Cu(3)	2.5135	2.6591	2.4382	2.623
Cu(3)-Cu(4)	2.5225	2.4564	2.4385	2.616
Cu(4)-Cu(5)	2.5185	2.6550	2.6440	2.623
Cu(5)-Cu(6)	2.5184	2.4448	2.4439	2.660
Cu(6)-Cu(1)	2.5234	2.6591	2.6472	2.616

Fig. S13 Optimized structures of metal core in **Au_2Cu_6PhMe** obtained by DFT calculation and crystal structure. The inset table shows the bond lengths in **Au_2Cu_6PhMe**.

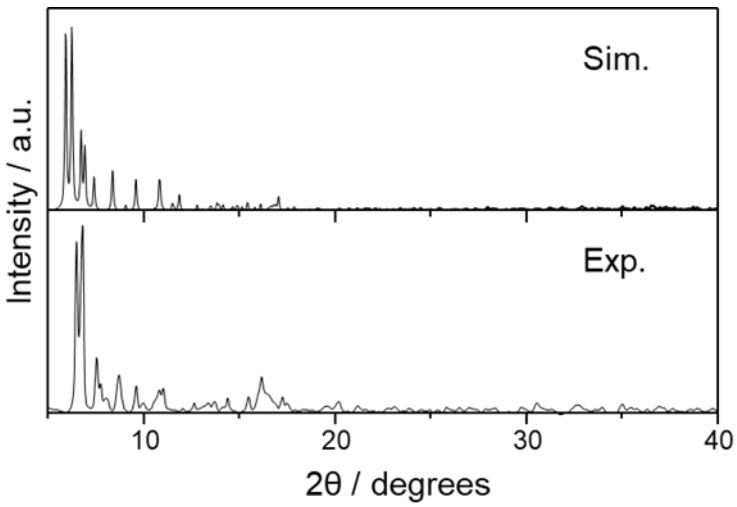

Fig. S14 Comparison of the experimental and simulated powder X-ray diffraction (PXRD) pattern of **Au_2Cu_6PhMe**. The experimental data was collected using a Cu-Kα radiation source, and the simulated pattern was generated from the single-crystal structure.

Supplemental Tables

Table S1. Crystallographic parameters for the crystal of $Au_2Cu_6(S\text{-}Adm)_6[P(PhMe)_3]_2$ (Au_2Cu_6PhMe).

	Au_2Cu_6PhMe
formula	$C_{102}H_{132}Au_2Cu_6P_2S_6$
formula weight	2387.62
crystal system	Triclinic
space group	$P\bar{1}$ (#2)
a (Å)	13.674(5)
b (Å)	15.457(6)
c (Å)	17.319(6)
α	66.822(10)
β	69.544(10)
γ	84.982(10)
V (Å^3)	3147(2)
Z	2
T (K)	120
λ (Å)	0.71073
R_{int}	0.0572
R_1 (I > 2.00σ(I)) [a]	0.0400
wR_2 (All reflections) [b]	0.1095
GOF	1.023
CCDC	2533432

[a] $R_1 = \Sigma(|F_o|-|F_c|)/\Sigma(|F_o|)$. [b] $wR_2 = [w(F_o^2-F_c^2)^2]/wF_o^2)^2]^{1/2}$.

Table S2. Comparison of photophysical parameters of Au_2Cu_6PhMe and Au_2Cu_6Ph nanoclusters in deaerated THF at room temperature, including emission maximum wavelengths (λ_{FL}, λ_{PH}), lifetimes (τ_{FL}, τ_{PH}), and quantum yields (Φ_{FL}, Φ_{PH}) of fluorescence and phosphorescence.

Nanocluster	λ_{FL} / nm	τ_{FL} / ns [a]	Φ_{FL}	λ_{PH} / nm	τ_{PH} / μs [a]	Φ_{PH}
Au_2Cu_6PhMe	685	2.4 (0.11%)	1.8×10^{-4}	819	5.5 (99.9%)	0.16
Au_2Cu_6Ph	679	9.0 (2.4%)	5.1×10^{-3}	825	4.9 (97.6%)	0.21

[a] Values in parentheses denote fractional population.

Table S3. Triplet lifetimes of perylene in deaerated THF containing different Au_2Cu_6PhMe sensitizer concentrations.

[**Au_2Cu_6PhMe**] / μM	τ_T / ms	β
5.4	0.261	0.59
10.7	0.256	0.50
15.6	0.249	0.54
20.1	0.246	0.57
24.9	0.242	0.50
30.4	0.237	0.50

Table S4. Emitter triplet lifetime in the absence of sensitizer (τ_{T0}) and quenching rate constant (k_q) and quenching efficiency (Φ_q) of excited-state emitter by sensitizer.

Sensitizer	Emitter	τ_{T0} / μs	k_q / $M^{-1}s^{-1}$	Φ_q [a]
Au_2Cu_6PhMe	perylene	267	1.56×10^7	0.02
PtOEP		1,090	2.12×10^7	0.03

[a] [**Au_2Cu_6PhMe**] = 5.73 μM; [PtOEP] = 1.43 μM.

Table S5. Measured and corrected upconversion quantum yields and their related parameters.

λ_{ex} / nm	Sensitizer	[Sen] / μM	Emitter	[Em] / mM	Φ_{TET}	$1-\Phi_q$	Φ_{UC}	Φ_{ISC}
532	**Au_2Cu_6PhMe**	5.73	perylene	5.0	0.33	0.98	0.01	0.55
	PtOEP	1.43			0.99	0.97	0.05	1

Table S6. Temperature dependence of photophysical parameters of Au_2Cu_6PhMe in THF solutions.

T / K	τ_f / ns	τ_p / μs	Φ_{PL}	Φ_{FL} / 10^{-4}	Φ_{PH}	Φ_{ISC}	Φ_{IC}
293	2.1	5.5	0.162	1.61	0.291	0.556	0.282
283	2.3	5.6	0.166	1.78	0.296	0.560	0.274
273	2.6	5.8	0.164	1.97	0.305	0.537	0.299
263	2.7	6.0	0.163	2.07	0.315	0.517	0.320

253	3.0	6.2	0.164	2.30	0.328	0.498	0.338
243	3.4	6.5	0.164	2.60	0.342	0.480	0.356
233	3.8	6.7	0.166	2.94	0.355	0.467	0.366
223	5.2	7.0	0.171	4.00	0.370	0.461	0.368
213	6.8	7.2	0.177	5.18	0.383	0.460	0.363
203	9.2	7.6	0.187	7.04	0.401	0.464	0.349
193	13.0	7.9	0.202	9.95	0.420	0.478	0.321

Table S7. Temperature dependence of radiative and non-radiative rate constants of Au_2Cu_6PhMe in THF solutions

T / K	k_{FL} / s^{-1}	k_{PH} / s^{-1}	k_{ISC} / 10^8 s^{-1}	k_{IC} / 10^8 s^{-1}
293			2.7	1.3
283			2.4	1.2
273			2.1	1.2
263			1.9	1.2
253			1.7	1.1
243	7.7×10^4	5.3×10^4	1.4	1.0
233			1.2	0.95
223			0.88	0.71
213			0.68	0.54
203			0.50	0.38
193			0.37	0.25

Table S8. Temperature dependence of photophysical parameters of Au_2Cu_6PhMe in the crystalline state.

T / K	λ_{FL} / nm	τ_{FL} / μs	τ_{PH} / μs	Φ_{PL}	Φ_{FL}	Φ_{PH} / 10^{-3}	Φ_{ISC}	Φ_{IC}
293	696	2.45	4.31	0.144	0.139	5.05	0.022	0.77
283	695	2.54	4.34	0.152	0.144	8.09	0.035	0.77
273	693	2.69	4.96	0.157	0.153	4.01	0.015	0.74
263	692	2.79	5.17	0.167	0.158	8.98	0.033	0.73

253	691	2.84	5.22	0.172	0.161	10.96	0.040	0.73
243	689	2.89	5.46	0.174	0.164	10.29	0.036	0.72
233	688	2.95	5.59	0.178	0.167	10.43	0.035	0.71
223	687	3.10	5.98	0.190	0.176	14.11	0.045	0.70
213	685	3.28	6.44	0.203	0.186	16.97	0.050	0.68
203	684	3.39	6.68	0.209	0.193	16.13	0.046	0.66
193	682	3.43	7.41	0.213	0.194	19.03	0.048	0.65

Table S9. Calculated excitation energies, oscillator strength (*f*), dominant configurations, and percentage contributions for the S_0-, S_1-, and T_1-optimized structures of Au_2Cu_6PhMe obtained by TD-B3LYP-D3/C-PCM (solvent = THF)//PCE0-GD3 calculations.

S_0-optimized structure				
Transition	Excitation energy / eV (nm)	f	Dominant configuration	Percentage contribution (%)
$S_0 \rightarrow S_1$	1.979 (627)	0.00176	H → L	88.1
$S_0 \rightarrow S_2$	1.983 (625)	0.00124	H → L+1	88.1
$S_0 \rightarrow T_1$	1.785 (695)	0	H → L	97.8
$S_0 \rightarrow T_2$	1.794 (691)	0	H → L+1	97.6
S_1-optimized structure				
$S_1 \rightarrow S_0$	1.723 (720)	0.00393	L → H	95.6
$S_2 \rightarrow S_0$	2.059 (602)	0.00159	L+1 → H	79.4
T_1-optimized structure				
$T_1 \rightarrow S_0$	1.485 (835)	0	L → H	98.5
$T_2 \rightarrow S_0$	1.784 (695)	0	L+1 → H	97.6

[a] The near-degeneracy of S_1 and S_2 vertical transitions at the S_0 geometry arises from the D_{3d} symmetry (degenerate LUMO/LUMO+1). Upon excitation, structural relaxation (Jahn-Teller-like distortion) lifts this degeneracy. At the S_1 optimized geometry, the S_1–S_2 energy gap widens to 0.34 eV, which is sufficiently large to prevent thermal population of S_2 at room temperature. This ensures that both ISC and emission occur exclusively from the relaxed S_1 state, consistent with Kasha's rule and the identical excitation profiles observed for FL and PH.

Table S10. Spin-orbit coupling matrix elements between the S_1 and T_n (n = 1 and 2) states in Au_2Cu_6PhMe obtained by ZORA/TD-B3LYP-D3/C-PCM (solvent = THF)//PCE0-GD3 calculations. [a]

n	$\langle T_n \lvert \hat{H}_{SO\,i} \rvert S_1 \rangle$ / cm^{-1}			$\lvert V_{SO} \rvert$ / cm^{-1} [b]
	i			
	x	y	z	
1 (H^1L^1)	5.31	1.35	12.4	7.8
2 (H^1L+1^1)	−61.7	−18.2	−1058.2	612.1

[a] Cartesian coordinate is defined in Fig. 4a. [b] Obtained using eqn (S16).

Table S11. Calculated intersystem crossing (ISC) rate constants and related parameters of Au_2Cu_6PhMe, obtained at the ZORA/TD-B3LYP-D3/C-PCM (solvent = THF) level.

ISC pathway	$\Delta E(S_1-T_n)$ / meV [a]	λ_{RE} / meV [b]	$\lvert V_{SO} \rvert$ / meV [c]	$k_{ISC}(S_1-T_n)$ / s^{-1} [d]
S_1-T_1	−250	37.6	0.97	7.3×10^5
S_1-T_2	155		75.9	7.6×10^{10}

[a] $\Delta E(S_1-T_n) = E_{Tn} - E_{S1}$ [b] Because the T_1 and T_2 states possess nearly identical electronic character, the reorganization energy for the S_1–T_2 ISC process was assumed to be identical to that calculated for the S_1–T_1 ISC. [c] Obtained using the S_1-optimized structure. [d] Calculated by eqn (S15).

Table S12. Summary of RMSD [Å] for the S_0, S_1, and T_1 stationary point geometries of Au_2Cu_6PhMe.

Classification	S_0-S_1 RMSD / Å	S_0-T_1 RMSD / Å	S_1-T_1 RMSD / Å
Metal core (Au_2Cu_6)	0.0636	0.0679	0.00427
Ligand	0.167	0.171	0.00394
Total	0.165	0.169	0.00395

References

(1) X. Kang, X. Li, H. Yu, Y. Lv, G. Sun, Y. Li, S. Wang, M. Zhu, *RSC Adv.* **2017**, *7*, 28606.
(2) M. J. Frisch, G. W. Trucks, H. B. Schlegel, G. E. Scuseria, M. A. Robb, J. R. Cheeseman, G. Scalmani, V. Barone, G. A. Petersson, H. Nakatsuji, *et al.*, *Gaussian 16, Revision B.01*, Gaussian, Inc., Wallingford CT, **2016**.
(3) J. Perdew, M. Ernzerhof, K. Burke, *J. Chem. Phys.* **1996**, *105*, 9982–9985.
(4) S. Grimme, J. Antony, S. Ehrlich, H. Krieg, *J. Chem. Phys.* **2010**, *132*, 154104.
(5) F. Weigend, R. B. Ahlrichs, *Phys. Chem. Chem. Phys*. **2005**, *7*, 3297–3305.
(6) M. M. Francl, W. J. Pietro, W. J. Hehre, J. S. Binkley, M. S. Gordon, D. J. DeFrees, J. A. People, *J. Chem. Phys.* **1982**, *77*, 3654–3665.
(7) D. Andrae, U. Häußermann, M. Dolg, H. Stoll, H. Preuß, *Theor. Chim. Acta* **1990**, *77*, 123.
(8) F. Neese, *WIREs Comput. Mol. Sci.* **2012**, *2,*73–78.
(9) F. Neese, *J. Chem. Phys.* **2005**, *122,* 034107.
(10) E. van Lenthe, E. J. Baerends, J. G. Snijders, *J. Chem. Phys.* **1994**, *101,* 9783–9792.
(11) E. van Lenthe, J. G. Snijders, E. J. Baerends, *J. Chem. Phys.* **1996**, *105,* 6505–6516.
(12) S. Grimme, *Wiley Interdiscip. Rev.: Comput. Mol. Sci.* **2011**, *1*, 211–228.
(13) F. Weigend, R. Ahlrichs, *Phys. Chem. Chem. Phys.* **2005**, *7,* 3297–3305.
(14) A. V. Marenich, C. J. Cramer, D. G. Truhlar, *J. Phys. Chem. B* **2009**, *113,* 6378–6396.
(15) S. Prathapan, S. I. Yang, J. Seth, M. A. Miller, D. F. Bocian, D. Holten, J. S. Lindsey, *J. Phys. Chem.*, *B* **2001**, *105*, 8237.
(16) D. Arima, Y. Niihori, M. Mitsui, *J. Mater. Chem. C* **2022**, *10*, 4597–4606.
(17) M. Mitsui, Y. Wada, R. Kishii, D. Arima, Y. Niihori, *Nanoscale* **2022**, *14*, 7974–7979.
(18) Y. Zhou, F. N. Castellano, T. W. Schmidt, K. Hanson, *ACS Energy Lett*. **2020**, *5*, 2322.
(19) E. M. Gholizadeh, L. Frazer, R. W. MacQueen, J. K. Gallahera, T. W. Schmidt, *Phys. Chem. Chem. Phys.* **2018**, *20*, 19500.
(20) J. Jortner, *J. Chem. Phys.* **1976**, *64*, 4860–4867.
(21) R. A. Marcus, *Rev. Mod. Phys.* **1993**, *65*, 599–610.
(22) D. Zhang, P. Pan, X. Du, X. Kang, M. Zhu, *Nanoscale* **2024**, 16, 11513–11517.